

3D ultrasound image segmentation using wavelet support vector machines

Hamed Akbari

Department of Radiology and Imaging Sciences, Emory University School of Medicine, Atlanta, Georgia 30329

Baowei Fei^{a)}

Department of Radiology and Imaging Sciences, Emory University School of Medicine, Atlanta, Georgia 30329; Department of Biomedical Engineering, Emory University and Georgia Institute of Technology, Atlanta, Georgia 30329; and Winship Cancer Institute of Emory University, Atlanta, Georgia 30329

(Received 21 December 2011; revised 9 April 2012; accepted for publication 11 April 2012; published 10 May 2012)

Purpose: Transrectal ultrasound (TRUS) imaging is clinically used in prostate biopsy and therapy. Segmentation of the prostate on TRUS images has many applications. In this study, a three-dimensional (3D) segmentation method for TRUS images of the prostate is presented for 3D ultrasound-guided biopsy.

Methods: This segmentation method utilizes a statistical shape, texture information, and intensity profiles. A set of wavelet support vector machines (W-SVMs) is applied to the images at various subregions of the prostate. The W-SVMs are trained to adaptively capture the features of the ultrasound images in order to differentiate the prostate and nonprostate tissue. This method consists of a set of wavelet transforms for extraction of prostate texture features and a kernel-based support vector machine to classify the textures. The voxels around the surface of the prostate are labeled in sagittal, coronal, and transverse planes. The weight functions are defined for each labeled voxel on each plane and on the model at each region. In the 3D segmentation procedure, the intensity profiles around the boundary between the tentatively labeled prostate and nonprostate tissue are compared to the prostate model. Consequently, the surfaces are modified based on the model intensity profiles. The segmented prostate is updated and compared to the shape model. These two steps are repeated until they converge. Manual segmentation of the prostate serves as the gold standard and a variety of methods are used to evaluate the performance of the segmentation method.

Results: The results from 40 TRUS image volumes of 20 patients show that the Dice overlap ratio is $90.3\% \pm 2.3\%$ and that the sensitivity is $87.7\% \pm 4.9\%$.

Conclusions: The proposed method provides a useful tool in our 3D ultrasound image-guided prostate biopsy and can also be applied to other applications in the prostate. © 2012 American Association of Physicists in Medicine. [<http://dx.doi.org/10.1118/1.4709607>]

Key words: image segmentation, prostate model, wavelet based texture extraction, kernel-based support vector machine, three-dimensional ultrasound imaging, transrectal ultrasound imaging, statistical shape model

I. INTRODUCTION

Ultrasound imaging provides portable, cost-effective, real-time imaging without exposure to radiation. It has been widely used for image-guided diagnosis and therapy. Ultrasound image segmentation for boundary delineation of the target object is a difficult task because of the uncertainty of the segmentation boundary caused by image speckle and because of a relatively low tissue-to-tissue contrast on the image.¹ Ultrasound segmentation is influenced by the quality of the data. Attenuation, shadows, and signal dropout due to the orientation dependence of image acquisition can result in missing boundaries and thus can cause problems in ultrasound segmentation.

Ultrasound imaging has been widely used for the management of prostate diseases. Prostate cancer is the second leading cause of cancer mortality in American men. It is estimated that there are 240 890 new cases and 33 720 deaths of prostate cancer in the United States in 2011.² Transrectal

ultrasound (TRUS)-guided biopsy is the gold standard for definitive diagnosis of the prostate. Currently, two-dimensional (2D) ultrasound images are used to guide a biopsy needle to take tissue sample for pathological examination. However, the current procedure is limited by 2D image guidance and does not have the capability for accurate, targeted biopsy of suspicious lesions in the prostate. Three-dimensional (3D) ultrasound image-guided biopsy systems are under evaluation for prostate diagnosis.^{3,4} Precise prostate segmentation in 3D ultrasound images has a key role in not only accurate placement of a biopsy needle but also many prostate-related applications. For example, the segmentation of the prostate will help physicians to plan brachytherapy for radiation seed implantation and to measure the volume of the prostate gland.

Segmentation of the prostate in ultrasound images can be difficult because of the shadows from the bladder, because of the relatively small size of the gland, and because of a low contrast between the prostate and non-prostate tissue. Many methods were proposed to automatically segment the

prostate in ultrasound images.^{5–24} Particularly, various shape model based methods are used to guide the segmentation. Gong *et al.* modeled the prostate shape using superellipses with simple parametric deformations.¹⁰ Ding *et al.* described a slice-based 3D prostate segmentation method based on a continuity constraint, implemented as an autoregressive model.⁸ Hu *et al.* used a model-based initialization and mesh refinement for prostate segmentation.²⁵ Hodge *et al.* described 2D active shape models for semiautomatic segmentation of the prostate and extended the algorithm to 3D segmentation using rotational-based slicing.²⁶ Tutar *et al.* proposed an optimization framework where the segmentation process is to fit the best surface to the underlying images under shape constraints.¹⁷ Zhan and Shen proposed a deformable model for automatic segmentation of the prostates from 3D ultrasound images using statistical matching of both shape and texture and Gabor support vector machines.²³ Ghanei *et al.* proposed a 3D deformable surface model for automatic segmentation of the prostate.⁹ Pathak *et al.* used anisotropic diffusion filter and prior knowledge of the prostate for the segmentation.¹⁵ Others proposed wavelet-based methods for the segmentation of the prostate. Knoll *et al.* used snakes with shape restrictions based on the wavelet transform for outlining the prostate.²⁷ Chiu *et al.* introduced a semiautomatic segmentation algorithm based on the dyadic wavelet transform and the discrete dynamic contour.⁷ Zhang *et al.* improved the prostate boundary detection system by tree-structured nonlinear filter, directional wavelet transforms and tree-structured wavelet transform.²⁴

Although advanced segmentation methods have been proposed for prostate ultrasound images, manual segmentation is the gold standard and is still used in many clinical applications because of reliability. However, manual segmentation is time consuming, highly subjective, and often irreproducible. Due to the low contrast between the prostate and nonprostate tissue and due to the low signal-to-noise ratio, there is still unmet clinical need to develop reliable, automatic, 3D segmentation methods for the prostate. In this research, we propose a new segmentation method for 3D prostate ultrasound images.

In this study, we focus on the use of texture features and statistical shape models for prostate segmentation. The extraction of texture feature within and around the prostate can be difficult. Many conventional image processing techniques do not perform well on TRUS images. The large variation in feature size and shape reduces the effectiveness of classical fixed neighborhood techniques. Textures at the prostate and nonprostate regions are similar in many cases. In other words, the distributions of texture features at the prostate and nonprostate regions may overlap with each other. Therefore, it is hard to linearly classify textures in TRUS images. Moreover, it is hard to define a global characterization of prostate textures because the same tissue may have variable texture in different zones of the prostate.

In our proposed segmentation method, our contribution includes the use of a wavelet support vector machine (W-SVM) and statistical shape model. A set of trained W-SVMs is employed to adaptively collect texture priors of

the prostates and differentiate tissue in different regions around the prostate by classifying the textures using wavelet transform features. Prostate shape statistics are incorporated in a shape model to modify the segmentation after the feature extraction step. Our method has two properties that improve the ability to classify the textures. First, the method employs several wavelet transform and each one extracts some aspects of the features. Second, these texture extractions were applied in three planes to classify the textures that are ambiguous in one plane in some regions. In our method, the large shape variation problem has been solved in three steps: (i) the method utilizes the texture extraction that is independent to the shape variability; (ii) a prostate probability model was employed that covers different shapes of the prostate; (iii) the manual box that was defined by the user will reconfirm the shape and location of the prostate. Human prostate images are used to validate the performance of the proposed segmentation method. Sections II and III describe the details of the methods and evaluation results, respectively.

II. METHODS

II.A. Overview of the segmentation method

A new 3D method is proposed to segment the prostate in 3D TRUS images. This method utilizes wavelet based texture extraction technique followed by kernel support vector machines (KSVMs) to adaptively collect texture priors of prostates and nonprostate tissues and classify tissues in different subregions around the prostate boundary by statistically analyzing their textures using wavelet features. Each W-SVM consists of two elements, i.e., wavelet filter collection and SVM. The wavelet filter collection is utilized to extract and characterize texture features in TRUS images. The wavelet filter collection has wavelet filters at multiscales and multiorientations. Therefore, it has the ability to characterize textures with different dominant sizes and orientations from noisy TRUS images. The KSVMs have been trained by a set of 3D TRUS image samples in coronal, sagittal, and transverse planes and at each subregion to label the voxels based on the captured wavelet texture features. Each voxel is labeled by three subregional KSVMs in three planes separately. Each voxel in each plane is labeled by a real value between 0 and 1 that represents the likelihood of a voxel belonging to the prostate tissue. A statistical prostate shape model is incorporated in the segmentation process. Therefore, each voxel has a label of the statistical shape model and three labels for KSVM in three planes. After defining special weight for each label at each region, each voxel tentatively labeled as prostate or nonprostate voxel. Consequently, the surfaces of the prostate are modified based on the intensity profiles of the model. The segmented prostate is updated and compared to the shape model. The modification and update steps are repeated until the algorithm converges.

Figure 1 shows the flowchart of the proposed segmentation method. The wavelet transforms are applied to 3D transrectal ultrasound images in three planes. The wavelet is used in 2D sagittal, coronal, and transverse images. The wavelet features are labeled by the locally trained SVM. After

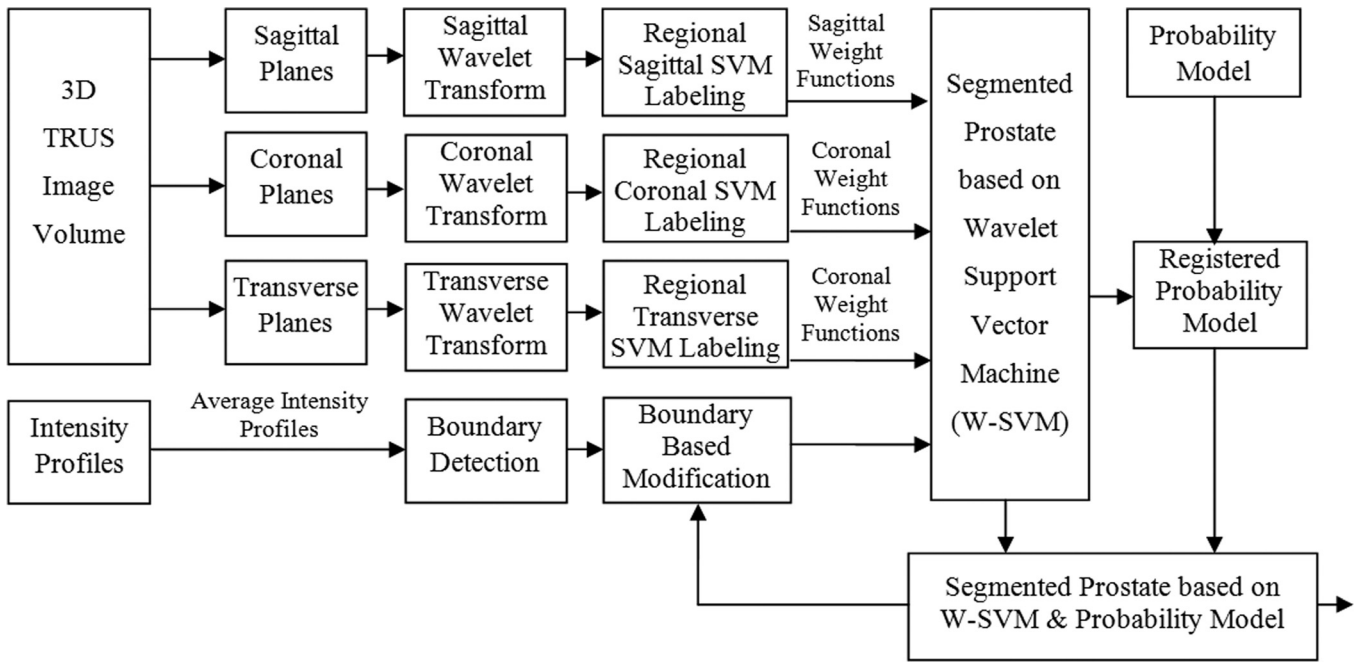


Fig. 1. Flowchart of the wavelet support vector machine (W-SVM) based segmentation method.

applying the weight functions that were defined in the SVM training step, the segmented prostate is used for registering the probability model. The weight function of the probability model is utilized to get the W-SVM. The result is modified using the intensity profiles. The last two steps are repeated until the algorithm converges. To improve the robustness of the method, a manual intervention was employed. This step was performed through defining a bounding box for the prostate in one middle slice or two orthogonal slices. The probability model was scaled to the size of the box as explained in Sec. II.D.

II.B. Wavelet-based texture extraction

Wavelet-based processing algorithms are superior due to the ability of wavelets to discriminate different frequencies and to preserve signal details at different resolutions. The capability of the wavelet filters to zoom in and out can translate signals to a location of a signal that is of interest and dilate themselves properly to preserve the resolution of that portion of the signal.²⁸

The transformed coefficients are two variable functions. The scaling and wavelet function are two functions, denoted by $\emptyset(x, y)$ and $\psi(x, y)$. The scaled and translated basis functions are defined as

$$\emptyset_{j,m,n}(x, y) = 2^{j/2}\emptyset(2^jx - m, 2^jy - n), \tag{1}$$

$$\psi_{j,m,n}^i(x, y) = 2^{j/2}\psi^i(2^jx - m, 2^jy - n), \quad i = \{H, V, D\}. \tag{2}$$

There are three different wavelet functions: $\psi_H(x, y)$, $\psi_V(x, y)$, and $\psi_D(x, y)$. Conceptually, the scaling function is the low frequency component of the previous scaling function in two dimensions. Therefore, there is one 2D scaling

function. However, the wavelet function is related to the order to apply the filters. The separable 2D basis functions can be expressed as the product of two 1D basis functions. Therefore, there are four basis functions for 2D signals as given in Eq. (2).

$$\begin{aligned} \emptyset(x, y) &= \emptyset(x)\emptyset(y) \\ \psi_H(x, y) &= \psi(x)\emptyset(y) \\ \psi_V(x, y) &= \emptyset(x)\psi(y) \\ \psi_D(x, y) &= \psi(x)\psi(y), \end{aligned} \tag{3}$$

where $\emptyset(x, y)$ is the 2D scaling function; $\psi_H(x, y)$, $\psi_V(x, y)$, $\psi_D(x, y)$ are the three 2D wavelet functions. For a 2D input signal, the transform coefficients are obtained by projecting the input onto the four basis functions given in Eq. (1). Therefore, discrete wavelet transform of function $f(x, y)$ are expressed as

$$W_\emptyset(j_0, m, n) = \frac{1}{\sqrt{MN}} \sum_{x=0}^{M-1} \sum_{y=0}^{N-1} f(x, y)\emptyset_{j_0,m,n}(x, y), \tag{4}$$

$$\begin{aligned} W_\psi^i(j, m, n) &= \frac{1}{\sqrt{MN}} \sum_{x=0}^{M-1} \sum_{y=0}^{N-1} f(x, y)\psi_{j,m,n}^i(x, y), \\ i &= \{H, V, D\}, \end{aligned} \tag{5}$$

where M and N are the sizes of the image.²⁹ Using a shift, multiply, and sum technique called convolution, wavelets can be combined with portions of an unknown signal to extract information from the unknown signal.³⁰

Using the wavelet transform, the texture properties can be characterized at multiple scales.³¹ For example, wavelet transform was used to characterize liver diseases from ultrasound

images.³² A texture is characterized by a set of channel variances estimated at the output of the corresponding filter bank. Ultrasound image textures can provide important features for accurately defining the prostate, especially for the regions where prostate boundaries are not clear.

Different types of wavelet transforms can be chosen for different applications. The implementation of the discrete wavelet frame transform is similar to that of the discrete wavelet transform, except that there is no down sampling operation.

Typical wavelet texture classification algorithms employ a wavelet that is optimal in some aspect. However, for some texture databases such as TRUS images, better classification results are obtained when using multiple wavelets. Therefore, in this study, biorthogonal wavelets 1.3 vertical details and first approximation, 1.5 vertical details and horizontal details, and 4.4 first approximation are employed to extract the texture features of the prostate. Choosing these wavelets is based on the ability of the segmentation of the TRUS images. Designing biorthogonal wavelets allows more degrees of freedom compared to orthogonal wavelets. One additional degree of freedom is the possibility to construct symmetric wavelet functions. A biorthogonal wavelet is not necessarily orthogonal. As in the orthogonal case, $\psi_1(t)$, $\psi_2(t)$, and $\phi(2t)$ are related by scaling functions, which are the consequence of the inclusions of the resolution spaces from coarse to fine. In the biorthogonal case, there are two scaling functions, which may generate different multiresolution analyses and, accordingly, two different wavelet functions. So, the numbers of coefficients in the scaling sequences may differ. Figure 2 shows five wavelet filters that were employed for feature extraction.

II.C. W-SVM

SVMs are supervised classifiers, which use a small number of exemplars selected from the tutorial dataset, with the intention to enhance the generalization ability. SVM has a pair of margin zones on both sides of the discriminate function. SVM is a popular classifier based on statistical learning theory as proposed by Vapnik.³³ The SVM framework is more appropriate for empirical mixture modeling, as nonseparable distributions of pure classes can be handled appropriately, as well as nonlinear mixture modeling.³⁴ The training phase of SVMs looks for a linear optimal separating hyperplane as a maximum margin classifier with respect to the training data. Since the training data are not linearly separable, kernel-based SVM methods are employed to classify the wavelet features. Kernel-based SVM methods map data from an original input feature space to a kernel feature space of higher dimensionality and then solve a linear problem in that space.³⁵ In this study, kernel-based SVM is used to identify the wavelet features of prostate tissue. Although these features may greatly vary among different patients, the SVMs nonlinearly classify texture features by extracting different wavelet features.

Since the prostate has different textures in different regions, a series of W-SVMs are assigned to different parts of the prostate in order to locally segment the prostate tissue. Therefore, each W-SVM segments a subregion of the pros-

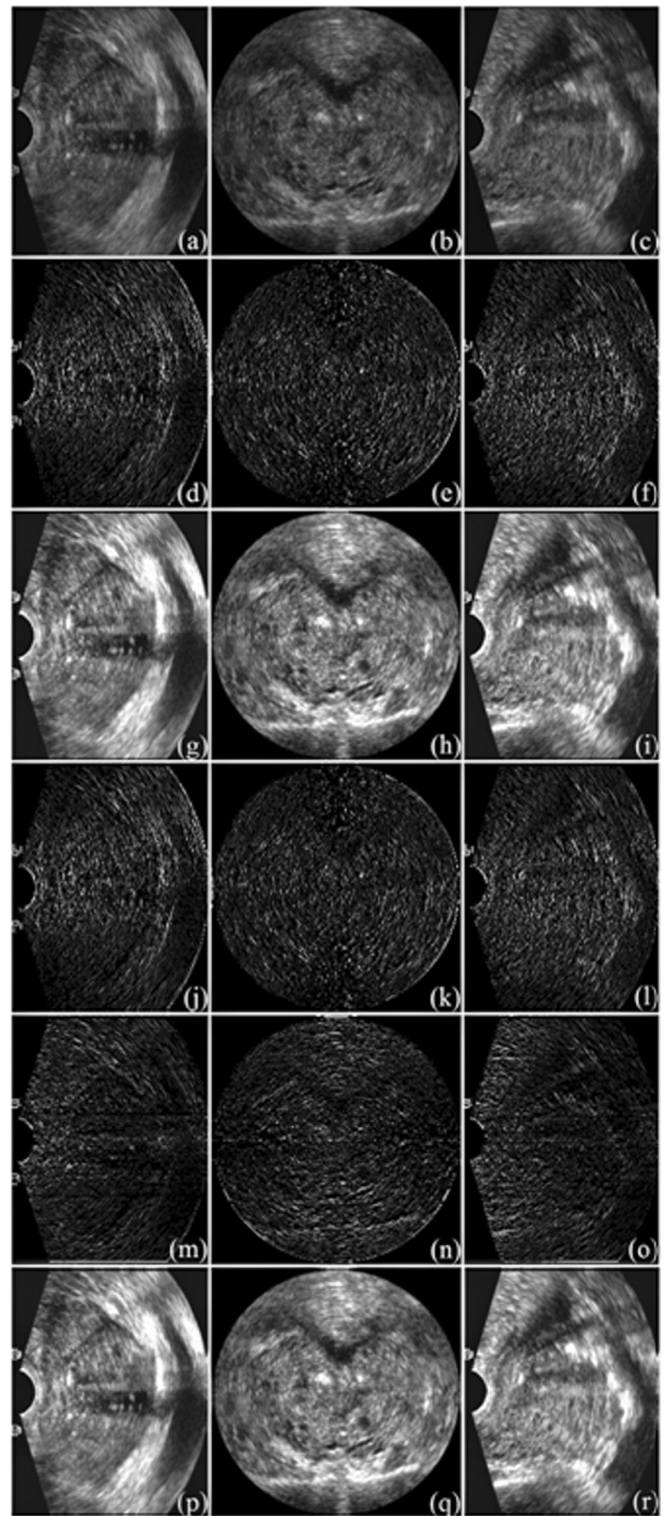


FIG. 2. Feature extraction using various wavelet filters. (a–c) Original images in sagittal, coronal, and transverse directions, respectively. (d–f) Biorthogonal 1.3 for vertical details in the corresponding images. (g–i) Biorthogonal 1.3 first approximation. (j–l) Biorthogonal 1.5 vertical details. (m–o) Biorthogonal 1.5 horizontal details. (p–r) Biorthogonal 4.4 first approximation.

tate with an intention to achieve robust classification of prostate texture features by kernel-based SVM. The method defines a hyperplane to classify the subjects by minimizing the following function:

$$\frac{1}{2}(w^T w + b^2) - C \sum_{i=1}^N \xi_i \tag{6}$$

subject to

$$y_i(w^T \phi(x_i) + b) \geq 1 - \xi_i, \quad \xi_i \geq 0, i = 1, \dots, N, \tag{7}$$

where C is a penalty parameter and ξ_i is slack variables to measure the deviation of training samples. w is the vector of coefficients and b is a constant offset. To find the optimal input parameter values, the grid search method is utilized. The index i labels the N training cases. $y \in \pm 1$ is the class label, and x_i is the independent variable. The kernel ϕ is used to transform data from the input to the feature space. There are number of kernels that can be used in SVM models. In our implementation, radial basis function (RBF) is employed as follows:

$$\phi = \exp(-\gamma|x_i - x_j|^2). \tag{8}$$

The RBF is one of the most popular kernel types employed in SVM. This kernel results in localized and finite responses across the full range of the real x-axis.

In the proposed segmentation procedure, the trained W-SVMs are employed to tentatively label voxels around the surface of the prostate as either prostate or nonprostate voxels. The W-SVMs are localized, trained, and employed at different regions and in the coronal, sagittal, and transverse planes. By using these tentatively labeled maps, the surface of the prostate can be delineated based on the boundary between the tentatively labeled prostate and nonprostate voxels in the three planes. For each voxel in each region, three weight functions are assigned corresponding to the segmentation in the three planes

$$W_s L_s + W_c L_c + W_t L_t, \tag{9}$$

where W_s , W_c , and W_t are weight functions in the sagittal, coronal, and transverse planes, respectively. L_s , L_c , and L_t are SVM labels in the sagittal, coronal, and transverse planes, respectively. These weight functions are obtained

from the optimization processing that finds the best result from ten manually segmented prostates. The weight functions are multipliers as described in Eq. (9), which are optimized by maximizing the function (9) for prostate voxels and by minimizing it for nonprostate voxels for the ten segmented prostates. Therefore, the optimization problem consists of maximizing or minimizing the function (9) by choosing input values from 0 to 1 and by computing the value of the function.

A number of W-SVMs on different regions of the surface model are placed and trained to adaptively label the tissue based on its texture and location. Each W-SVM is composed of five wavelet filter banks, voxel coordinates, and a kernel-based SVM. Figure 3 shows the flowchart of the training step to calculate the weight functions and to train the SVMs in each region. The segmented prostate is modified based on the probability model and the intensity profiles. By repeating these steps of voxel labeling and model-based deformation, the method is able to segment the prostate.

II.D. Probability shape model

The probability prostate model is created using ten manually segmented prostate. These ten binary 3D images are registered through the principle axis transformation. The registered models are overlaid together and create a probability model of the prostate, within which each pixel is labeled with a value between 1 and 10. The principal axis transformation is inspired from the classical theory of rigid bodies.³⁶ A rigid body can be uniquely localized by defining the coordination of its center of mass and its orientation with respect to its center of the mass. For any rigid body, the center of mass and principal axes can be determined based on the geometry of the object. For symmetric geometries, axes of symmetry are the same as the principal axes and, in general, form an orthogonal coordinate system, with their origin at the center of mass.³⁷ The inertia matrix in the principal axis coordinate system is diagonal. Let us consider two orientations and locations for a volume with no assumptions about the orientation or location of the reference volumes. If the reference volumes represent the same object, the centers of mass C_1 and C_2 will represent the same physical point in the

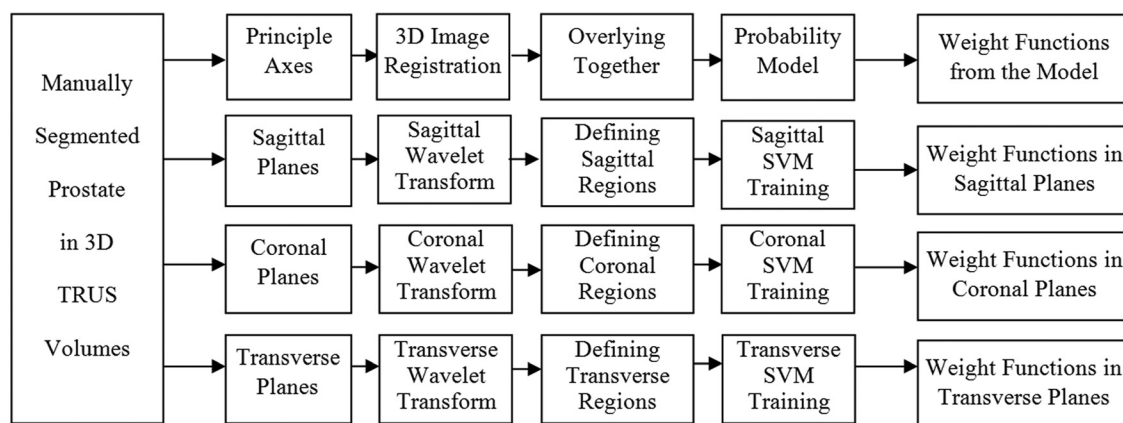


FIG. 3. Flowchart of the training for the support vector machines (SVMs) in three orthogonal planes from the manually segmented prostate images.

object, independent of orientation or scale. The inertia matrices, I_i , for the two reference volumes can be expressed as a similarity transformation

$$I_i = S_i I S_i^T, \tag{10}$$

where I is the inertia matrix in the principal axis coordinate system, S_i is the rotation matrix that is the matrix of eigencolumns determined from I_i , and the eigencolumns are orthonormal vectors directed along the principal axes. This equation geometrically represents a rotation of I relative to the original image coordinate axes. I_1 and I_2 are related by the following equation:

$$I_2 = S_2 S_1^T I_1 S_1 S_2^T. \tag{11}$$

Registration of image 1 to image 2 can be obtained by a translation to the center of mass coordinate system followed by the rotation $S_1 S_2^T$. Then, the size of 3D prostate images is scaled in three axes based on principle axes lengths. After registration, the prostate models overlay together, and the shape probability model is created based on the number of overlaying prostates in each voxel. Figure 4 shows the probability model in three planes and at different sections.

II.E. Intensity profile model

An average model of intensity profiles is created using the intensity profiles of the ten training 3D prostate images. Let L_p ($p = 1, \dots, 10$) be the intensity profile along the lines passing through the center of mass of the prostate and including both sides of the prostate boundary

$$L = \frac{1}{4l^2} \sum_{i=-l}^{i=l} \sum_{j=-l}^{j=l} I_{B-k}^{B+k}, \tag{12}$$

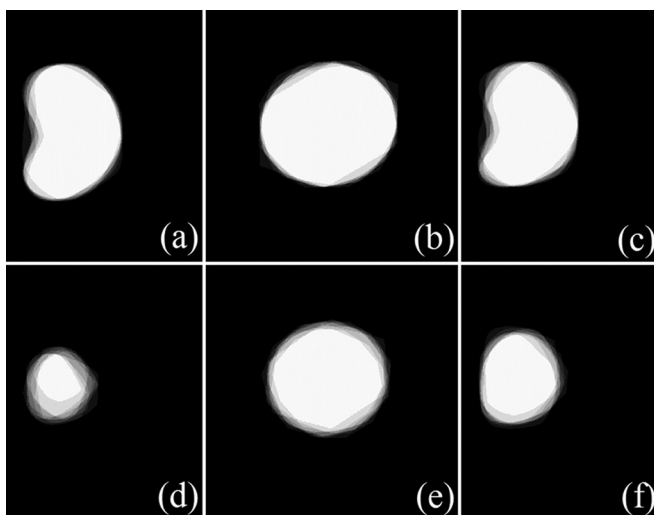


Fig. 4. 3D probability shape model of the prostate in the sagittal (left panel), coronal (center panel), and transverse (right panel) directions. The intensity represents the probability of the voxel that belongs to prostate tissue with a probability range from 100% (white) to zero (dark). The top and bottom rows represent different slice positions.

where I is a voxel intensity, i and j are two orthogonal directions regarding to the profile axis, $2l$ is the profile width, $2k$ is the profile length, and B is the location of the boundary of the prostate in the profile. The profiles are evaluated in all angles and with different widths. Considering just one single line of voxels, very noisy results are obtained. Figure 5 shows the center of mass of a prostate and the intensity profile with a width of nine voxels. Figure 6 shows the intensity profile with different cube widths. When the width increases, the intensity profile shows more consistent shape in different patients. Therefore, the profile width is increased to find a consistent intensity profile shape among all prostates. Figure 7 shows a sample of intensity profiles in three orthogonal directions. The width of the cubes is 101 pixels and the profiles pass through the center of mass of the prostate. The profiles are parallel with sagittal, coronal, and transverse planes. Using ten prostate models, average intensity profiles were generated across the prostate boundaries. Next, the similarity of the intensity profiles in the experimental cases is compared with the model to identify the prostate boundary. These detected points are then incorporated into the segmentation scheme as described above.

II.F. Evaluation criteria

Quantitative performance assessment of the method was done by comparing the results with the corresponding gold standard from manual segmentation. The Dice similarity was employed as a performance assessment metric for the prostate segmentation algorithm. The Dice similarity was computed as follows:

$$\text{Dice}(S, G) = \frac{2|S \cap G|}{|S| + |G|} \times 100\%, \tag{13}$$

where S represents the voxels of the prostate segmented by the algorithm and G represents the voxels of the corresponding gold standard from manual segmentation.

The volume error was used as another performance assessment metric to evaluate the prostate segmentation algorithm. Volume error, $\text{VE}(S, G)$, represents the signed volume error of a segmented prostate volume, S , compared to the gold standard, G , as a percentage of the gold standard prostate volume, which is described below:³⁸

$$\text{VE}(S, G) = (S - G)/G \times 100\%. \tag{14}$$

Sensitivity, $\text{Sen}(S, G)$, represents the proportion of the segmented prostate volume, S , that is correctly overlapped with the gold standard volume, G

$$\text{Sen}(S, G) = \text{TP}/G \times 100\%, \tag{15}$$

where TP is the true positive volume and represents the overlapped volume of the segmented prostate and the gold standard.

False negative rate (FNR) is another evaluation criterion. When a voxel was not detected as a prostate voxel, the

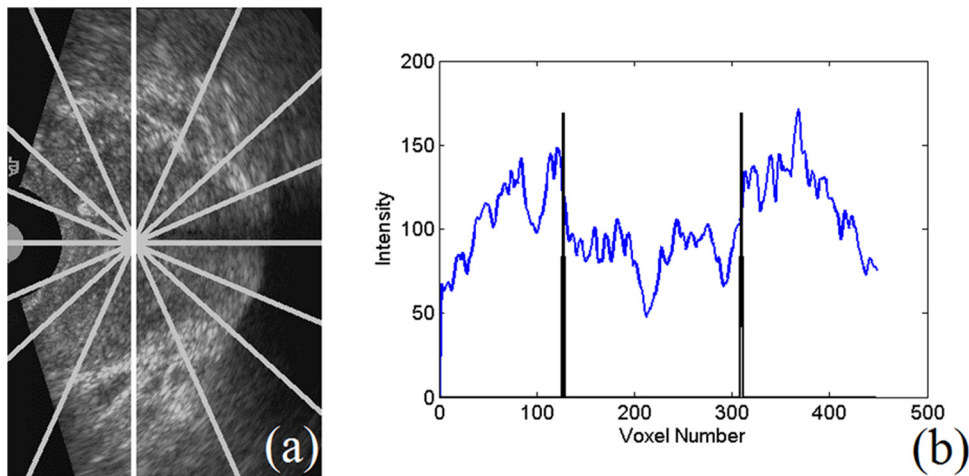


FIG. 5. Left: Example ultrasound image of the prostate that shows the center of mass and the cubes passing through the center with different angles. Right: Intensity profile corresponding to the white cube in the image on the left. Black vertical lines show the location of the prostate boundaries.

detection was considered a false negative if the voxel was a voxel of prostate on the gold standard that was established by manual segmentation. The FNR was defined as the number of false negative voxels divided by the total number of

the prostate voxels on the gold standard. The gold standard is a binary image consisting of voxels that are labeled as prostate and other voxels that are assumed as nonprostate voxels.

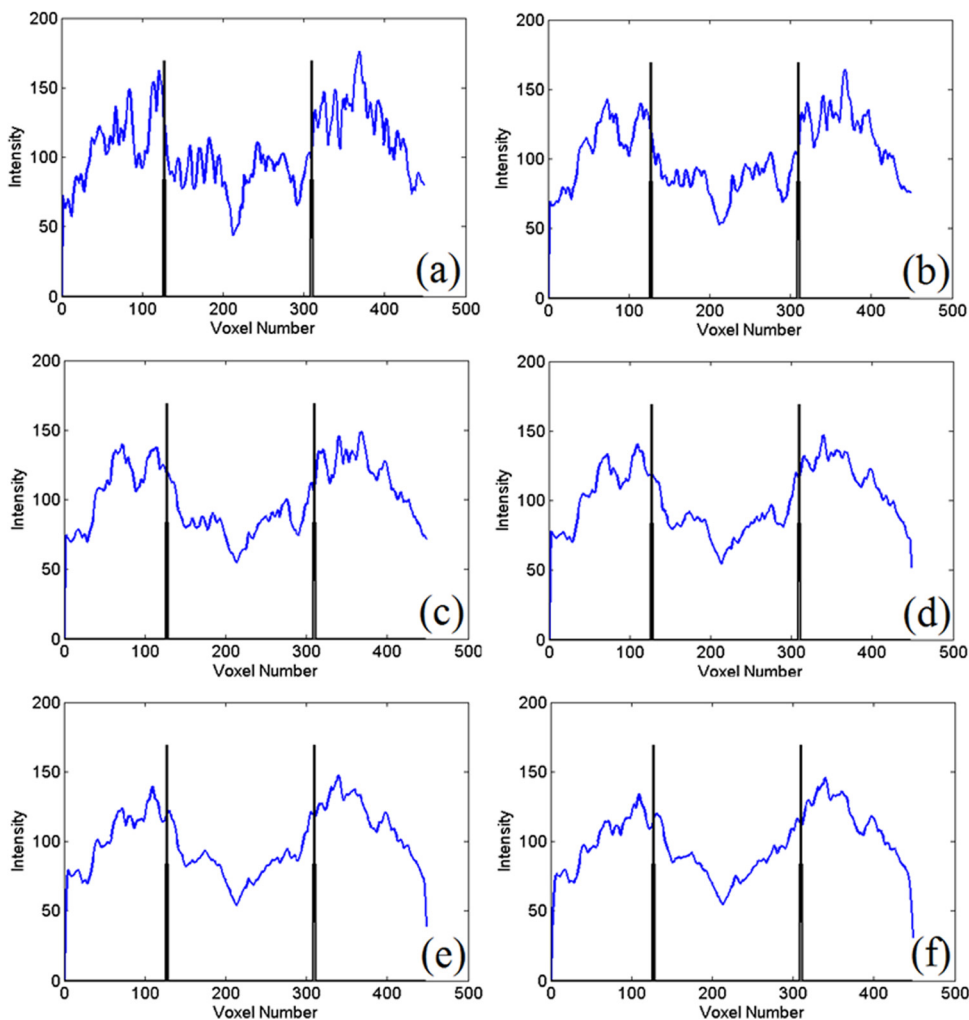


FIG. 6. Changes in intensity profiles with respect to the width of the cube [(a) 3 voxels, (b) 19 voxels, (c) 39 voxels, (d) 59 voxels, (e) 79 voxels, and (f) 99 voxels]. Black vertical lines in the graphs show the location of the prostate boundaries.

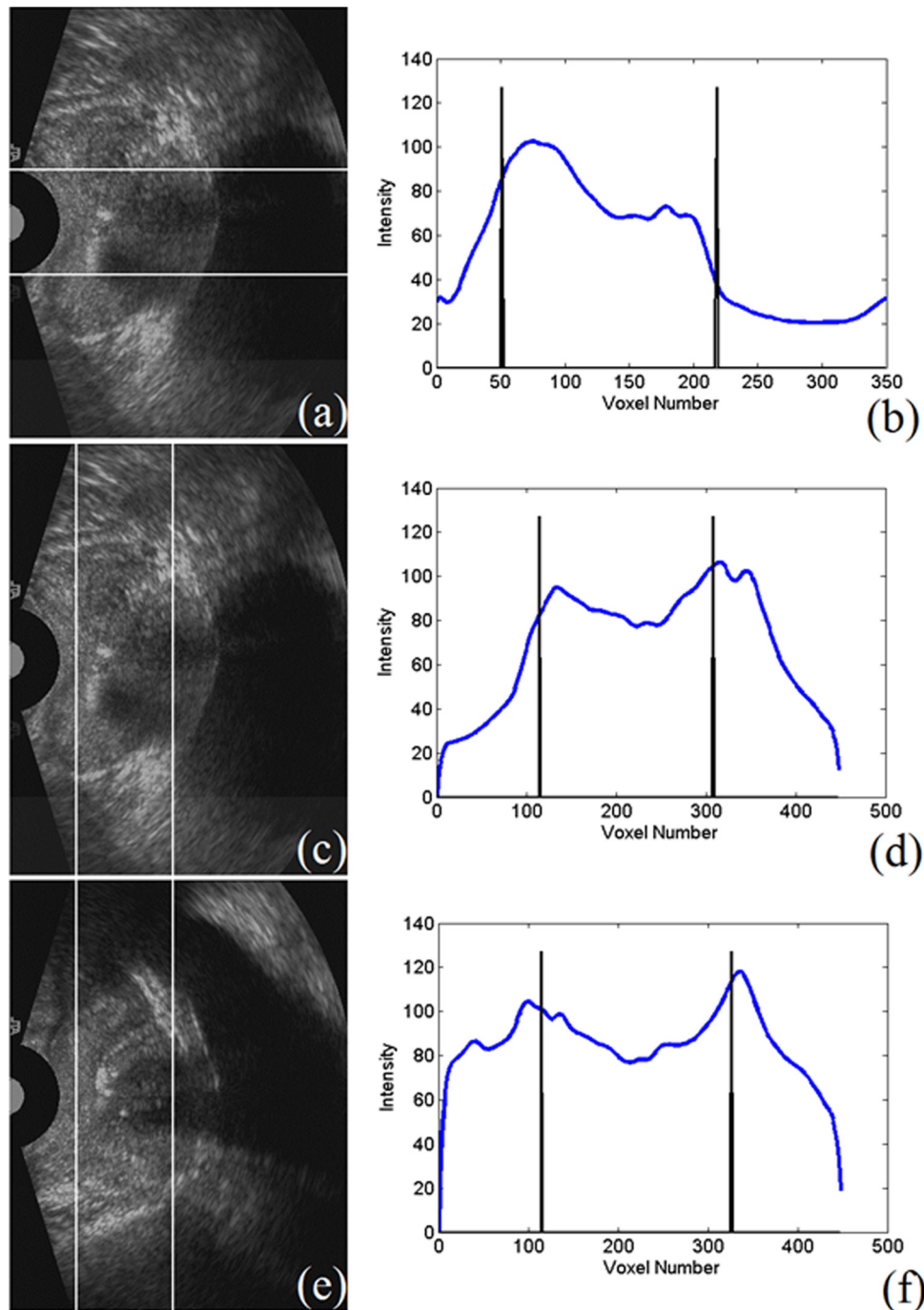


FIG. 7. Prostate ultrasound images (left) and the corresponding intensity profiles (right) of the cubes passing through the prostate in three orthogonal directions. The white lines on the images show the cube boundaries. The black vertical lines on the profiles show the location of the prostate boundaries.

Error ratio represents the proportion of the volume that is not correctly overlapped with the gold standard volume. As is shown in Eq. (18), false positive volume and false negative volume are the key parts of the calculation method

$$ER(S, G) = \frac{FP + FN}{G + S} \times 100\%, \quad (16)$$

where FP and FN are false positive and false negative, respectively.

III. EXPERIMENTAL RESULTS

The proposed 3D segmentation method was applied to 40 transrectal ultrasound image volumes from 20 patients. The TRUS images were acquired from patients who were clinically selected to undergo the prostate biopsy procedure. An HDI-5000 ultrasound system and an end-firing 5–9 MHz TRUS transducer probe were used for the image acquisition. Each patient has two image volumes acquired at different times. The voxel size of the image is $0.19 \times 0.19 \times 0.19$ mm³. The size of the images is $448 \times 448 \times 350$ voxels. The

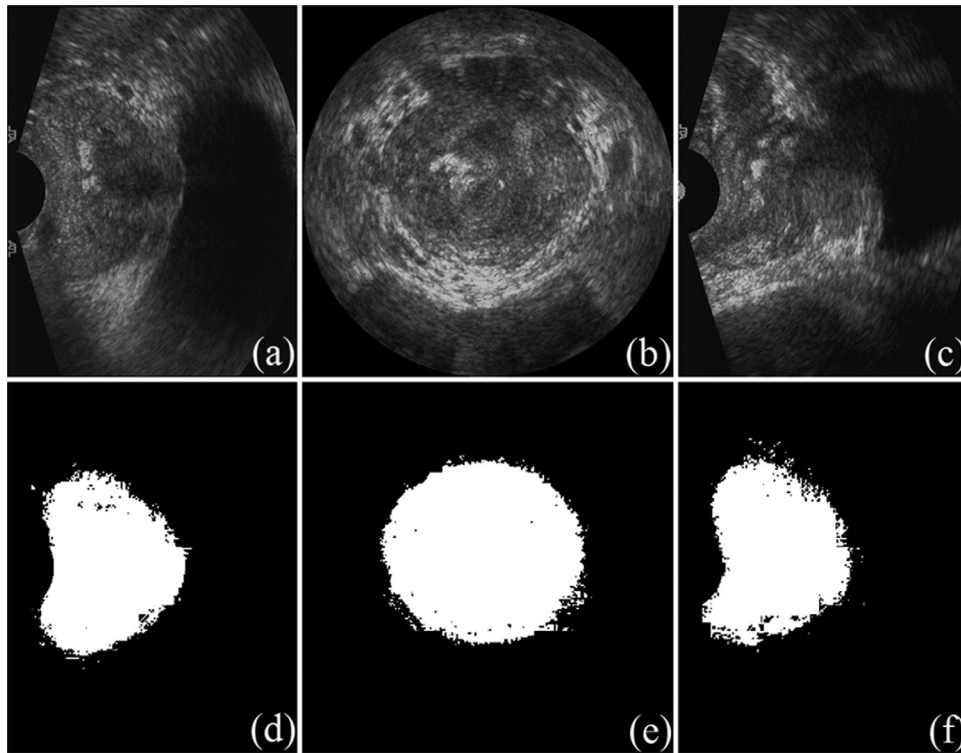


FIG. 8. Segmentation result of the prostate using the wavelet support vector machines method. (a–c) Original image in the sagittal, coronal, and transverse directions, respectively. (d–f) Segmented prostate in the three corresponding images.

prostate was manually segmented by drawing the prostate boundaries on individual image slices.

The experimental data set differed from the training set. Four slightly different approaches were applied to segment the prostate. They include (1) W-SVM; (2) the probability shape model-based W-SVM (MW-SVM); (3) MW-SVM plus one bounding box for the prostate (MW-SVM1). The user placed one bounding box in one image slice. The algorithm assumes that the prostate is located within the box. (4) MW-SVM with two bounding boxes for the prostate (MW-SVM2). The user placed two bounding boxes in two orthogonal image slices. The algorithm assumes that the prostate is located within the two orthogonal boxes.

Figure 8 shows the segmentation result of a typical image volume of the prostate using the W-SVM segmentation

method. As shown in the images, the segmented prostate presents the shape of the actual organ. Without the probability shape model, the boundaries are not smooth and noise appears around the boundary region.

The MW-SVM performs well (Fig. 9). The segmented boundaries are close to those by manual segmentation gold standard. Figure 10 shows the 3D overlay visualization of the automatic and manual segmentation of the prostate, indicating an excellent overlap between two segmented results in three dimensions.

Table I shows the quantitative evaluation results from 40 image volumes. With a simple user intervention, i.e., placing two bounding boxes for the prostate, the quality of the segmentation was improved significantly. The Dice overlap ratios were increased from $74.5\% \pm 9.5\%$ for the MW-SVM

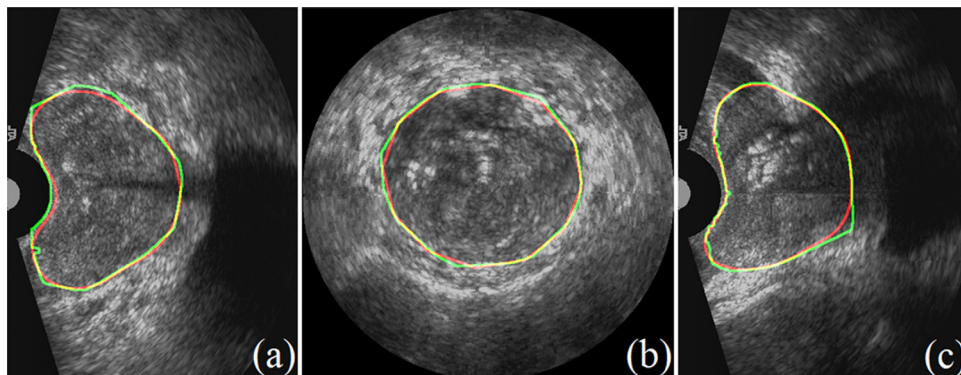


FIG. 9. Prostate segmentation results in sagittal (left), coronal (center), and transverse (right) directions. On each image, the boundary from the automatic segmentation is close to the smooth boundary from the manual gold standard.

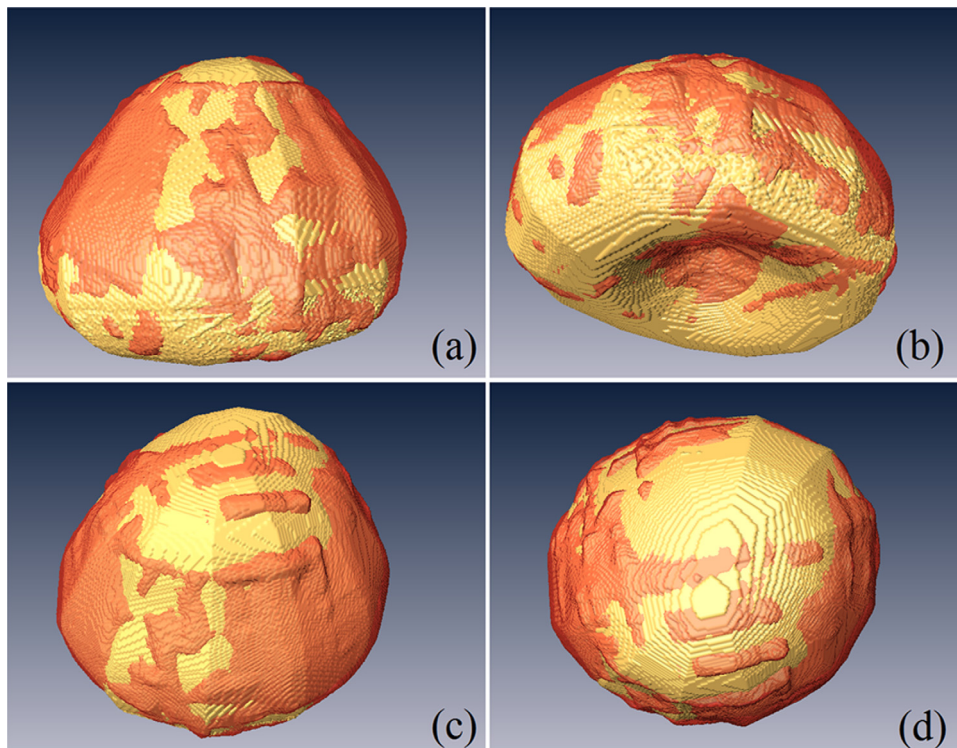


FIG. 10. Three-dimensional visualization of the segmented prostate (darker region) as compared to the manual gold standard (brighter region) in four different views (a–d) of the same human prostate.

method to $90.3\% \pm 2.3\%$ for the MW-SVM2 method. The minimum of Dice ratio is 87.2% for MW-SVM2, indicating that the method can reliably segment all the 40 prostates with a relatively high accuracy. The probability shape model also improves the quality of the segmentation but not dramatically. After the use of the shape model, the Dice overlap ratios were increased by only 2.7% .

For the MW-SVM2 method, the sensitivity is $87.7\% \pm 4.9\%$ and the false positive rate is $0.5\% \pm 0.2\%$, indicating the method can detect prostate tissue with a relatively low error. The mean volume error is $6.6\% \pm 3.6\%$, which demonstrates that the measurement of prostate volume is accurate as compared to the manual segmentation gold standard.

To estimate the importance of the bounding box and the probability model, a simple experiment was performed. The probability model was located in the user defined bounding box and the probabilities more than 50% were assumed as the prostate. The Dice ratio in this experiment is $88.6 \pm 1.7\%$

($82.6\%–90.7\%$) which shows the importance of combining the W-SVM, the probability model, and the bounding box.

The method has been evaluated through multiple rounds of cross validation by utilizing different partitions of training and testing image groups. Fifty TRUS images were randomly divided into five groups and each group has ten images. The method has been evaluated in five rounds. In each round, one group of ten images has been utilized for training and the other four groups of 40 images have been used to test the method. Table II shows the numerical results of these evaluations, which indicate the robustness of the segmentation method.

IV. DISCUSSION

In this paper, we proposed a W-SVM and a statistical shape model for prostate segmentation in transrectal ultrasound images. The model-based W-SVM segmentation method successfully segmented all 40 prostate ultrasound images.

TABLE I. Quantitative evaluation of four segmentation methods: (1) W-SVM; (2) model-based W-SVM (MW-SVM); (3) MW-SVM plus one bounding box for the prostate (MW-SVM1). The user places one bounding box in one image slice. The algorithm assumes that the prostate is located within the box. (4) MW-SVM with two bounding boxes for the prostate (MW-SVM2). The numbers are described as mean \pm standard deviation (minimum–maximum) of 40 prostate image volumes in percentage.

Methods	MW-SVM2	MW-SVM1	MW-SVM	W-SVM
Dice overlap ratio (%)	90.3 ± 2.3 (87.2–94.7)	81.2 ± 8.3 (62.0–93.8)	74.5 ± 9.5 (56.3–90.8)	71.8 ± 10.2 (53.5–91.2)
Sensitivity (%)	87.7 ± 4.9 (78.9–96.9)	79.5 ± 9.0 (58.5–95.7)	77.6 ± 17.0 (39.2–99.5)	73.3 ± 17.4 (39.6–97.9)
False negative rate (%)	12.3 ± 4.9 (3.1–21.2)	20.5 ± 9.1 (4.3–41.5)	22.4 ± 17.0 (0.5–60.8)	26.7 ± 17.4 (2.1–60.5)
Volume error (%)	6.6 ± 3.6 (0.4–12.3)	16.3 ± 9.7 (1.4–40.2)	29.6 ± 20.8 (0.0–88.5)	29.3 ± 19.4 (0.3–76.2)
Error ratio (%)	9.7 ± 2.2 (5.3–12.9)	18.8 ± 8.3 (6.2–38.0)	25.5 ± 9.5 (9.2–43.7)	28.2 ± 10.2 (8.8–46.5)

TABLE II. Cross validation results of five partitions of training and test subjects. The numbers are described as mean \pm standard deviation (minimum–maximum) of 40 prostate image volumes in percentage.

Rounds	1	2	3	4	5
Dice overlap ratio (%)	90.3 \pm 2.1 (82.8–93.9)	91.2 \pm 2.2 (81.4–94.5)	91.3 \pm 2.2 (82.0–94.5)	90.9 \pm 2.0 (81.5–93.9)	90.8 \pm 1.7 (86.9–94.1)
Sensitivity (%)	93.6 \pm 2.1 (88.2–97.6)	89.3 \pm 2.9 (84.8–95.2)	92.6 \pm 2.6 (87.4–97.8)	91.8 \pm 2.4 (87.4–96.9)	94.0 \pm 2.0 (90.2–97.3)
False negative rate (%)	6.4 \pm 2.1 (2.4–11.8)	10.4 \pm 2.9 (4.8–15.2)	7.4 \pm 2.6 (2.2–12.6)	8.2 \pm 2.4 (3.1–12.6)	6.0 \pm 2.0 (2.7–9.8)
Volume error (%)	13.8 \pm 5.2 (5.2–32.0)	6.4 \pm 4.2 (26.8–1.5)	10.2 \pm 5.0 (3.4–30.3)	10.3 \pm 4.8 (3.2–30.4)	13.0 \pm 4.1 (5.3–22.3)
Error ratio (%)	9.7 \pm 2.1 (6.1–17.2)	8.7 \pm 2.2 (5.5–18.6)	8.7 \pm 2.2 (5.6–18.0)	9.1 \pm 2.0 (6.1–18.5)	9.2 \pm 1.7 (5.9–13.1)

Although others have previously proposed methods to segment the prostate in TRUS images, most of the methods have been used to segment the prostate in 2D images. Only a few papers have been published to segment the prostate in 3D TRUS images. The advantage of our method is the combination of texture information and geometrical knowledge for prostate segmentation.

Previously, Tutar *et al.* proposed a method for 3D TRUS segmentation that was defined in an optimization framework as fitting the best surface to the underlying images using shape constraints.³⁹ To derive these constraints, the method modeled the shape of the prostate using spherical harmonics of degree eight and performed statistical analysis on the shape parameters. After user initialization, the algorithm identifies the prostate boundaries. This method was evaluated in 30 TRUS images to segment the prostate. By assuming the average of manual boundaries as the ground truth, the method computed the segmentation error. The percent volume overlap was 82.8% \pm 6.2%.

In another study, Ghanei *et al.* proposed a discrete structure model made from a set of vertices in the 3D space that form triangle facets.⁹ The model converges from an initial shape to its equilibrium iteratively, by a weighted sum of the internal and external forces. Internal forces are based on the local curvature of the surface and external forces are extracted from the volumetric image data by applying an appropriate edge filter. The method applied the proposed deformable model to segment the prostate in ten ultrasound image sets. The average similarity was 88.58% and the average difference was 11.42%.

In a recent study, the concept of an ignorance function was used to determine the best threshold with which to binarize an image in order to segment the prostate.⁴⁰ The approach introduced a method to construct such functions from t-norms and automorphisms. By means of these new measures, the method represented the degree of ignorance of the expert when given one fuzzy set to represent the background and the other to represent the object. This method was able to segment the prostate with an error of 15%–20%.

Several features of the proposed segmentation method contribute to the accuracy and robustness of the algorithm. First, the use of wavelet transform for texture extraction is important for the segmentation method. The segmentation approach was partially inspired by physician's manual segmentation where prostate texture definition, boundary evaluation, and anatomical knowledge are combined to differentiate prostate and nonprostate tissue. In this algorithm, wavelet transform

was employed to extract the texture features in ultrasound images. Intensity profile was utilized to modify the boundary. The probability model was used as the anatomical knowledge. Texture analysis is mainly used to segment the image into some homogeneous subregions. Texture properties can then be characterized by the spatial distribution of gray levels in a neighborhood and are utilized to determine regional homogeneity. Texture extraction using wavelet transform can provide a precise and unifying frame work for the analysis and characterization of a signal at different scales.⁴¹ The selection of the appropriate wavelet transforms was based on the best results for prostate classification. Different types of wavelet transform were applied and classified using SVM. The best results were chosen for texture extraction. The method particularly includes a set of trained SVMs to adaptively collect texture priors of the prostates and to differentiate tissues in different zones around the prostate boundary by statistically analyzing their textures.

Second, the kernel-based support vector machine is a key component of the segmentation algorithm. The inputs of each kernel-based SVM consist of wavelet transformations components. Since the prostate textures are different in different regions of the prostate, the W-SVMs were locally trained and employed in order to characterize texture features in ultrasound images. Since the wavelet filter bank has different wavelets transform, it is able to characterize textures with different dominant sizes and orientations from noisy ultrasound images.

Third, the intensity profiles and the probability shape model are an integral part of the segmentation algorithm. We expect that the prostate has geometry and location information with a series of constraints. These constraints were incorporated in the probability model. The model prevents significant variations from the popular shape. The model modifies the segmentation based on prostate anatomical knowledge. The intensity profiles were used to improve the segmentation based on boundary detection. As the ultrasound images are noisy, the profiles from a large cube that passes through the prostate help to locate prostate boundaries. When the cube has a smaller diameter, the intensity profile is noisy and not consistent among patients. When the cube is large with a diameter about 100 voxels, the profile becomes smooth and thus it is easier to locate the prostate boundary.

Fourth, the manual selection of two bounding boxes for the prostate is a simple step but it is important to improve the segmentation results. This was easily implemented by quickly viewing the image volume to locate the location of

the prostate before the automatic segmentation. The 3D segmentation takes 2–3 min for a desktop computer with 16 GB RAM and 3.40 GHz (4 Core) processor using MATLAB code. The time can be reduced to a few seconds in a high-performance PC with graphical processing unit (GPU) and with C code.

V. CONCLUSION

A set of W-SVMs and a statistical shape model are developed and evaluated for ultrasound prostate image segmentation. Wavelet transform was employed for prostate texture extraction. W-SVMs are located at different regions of the prostate surface in order to classify prostate and nonprostate tissue. The W-SVM method employs a learning mechanism to automatically collect texture features in different regions of the prostate. Compared to 2D prostate segmentation methods, the proposed method can segment the prostate in three dimensions. The segmentation method with support vector machines and wavelet transform can be applied to various applications in not only the prostate but also other organs.

ACKNOWLEDGMENTS

This research was supported in part by NIH Grant No. R01CA156775 (PI: Fei), Georgia Cancer Coalition Distinguished Clinicians and Scientists Award (PI: Fei), Emory Molecular and Translational Imaging Center (NIH Grant No. P50CA128301), SPORE in Head and Neck Cancer (NIH Grant No. P50CA128613), and Atlanta Clinical and Translational Science Institute (ACTSI) that is supported by the PHS Grant No. UL1 RR025008 from the Clinical and Translational Science Award program. The authors thank Dr. Aaron Fenster for providing the ultrasound images, Mr. Xiaofeng Yang and Ms. Luma Halig for discussions, and Ms. Jessica Paulishen for editing the English.

^{a)} Author to whom correspondence should be addressed. Electronic mail: bfei@emory.edu; Telephone: 404-712-5649; Fax: 404-712-5689.

¹J. A. Noble and D. Boukerroui, "Ultrasound image segmentation: A survey," *IEEE Trans. Med. Imaging* **25**, 987–1010 (2006).

²R. Siegel, E. Ward, O. Brawley, and A. Jemal, "Cancer statistics, 2011: The impact of eliminating socioeconomic and racial disparities on premature cancer deaths," *CA Cancer J. Clin.* **61**, 212–236 (2011).

³B. Fei, V. Master, P. Nieh, H. Akbari, X. Yang, A. Fenster, and D. Schuster, "A PET/CT directed, 3D ultrasound-guided biopsy system for prostate cancer," *Prostate Cancer Imaging. Image Analysis and Image-Guided Interventions*, Lecture Notes in Computer Science (Springer-Verlag, Berlin, Heidelberg, 2011), Vol. 6963, pp. 100–108.

⁴J. Bax, J. Williams, D. Cool, L. Gardi, J. Montreuil, V. Karnik, S. Sherebrin, C. Romagnoli, and A. Fenster, "Mechanically assisted 3D prostate ultrasound imaging and biopsy needle-guidance system," in *Medical Imaging 2010: Visualization, Image-Guided Procedures, and Modeling*, Vol. 7625, edited by K. H. Wong and M. I. Miga (SPIE, San Diego, CA, 2010).

⁵H. Akbari, X. Yang, L. Halig, and B. Fei, "3D segmentation of prostate ultrasound images using wavelet transform," *Medical Imaging - Image Processing*, edited by Benoit M. Dawant and David R. Haynor, *Proc. SPIE* **7962**, 79622K-1–79622K-8 (SPIE, San Diego, CA, 2011).

⁶N. Betrouni, M. Vermandel, D. Pasquier, S. Maouche, and J. Rousseau, "Segmentation of abdominal ultrasound images of the prostate using a priori information and an adapted noise filter," *Comput. Med. Imaging Graph.* **29**, 43–51 (2005).

⁷B. Chiu, G. H. Freeman, M. M. A. Salama, and A. Fenster, "Prostate segmentation algorithm using dyadic wavelet transform and discrete dynamic contour," *Phys. Med. Biol.* **49**, 4943–4960 (2004).

⁸M. Y. Ding, B. Chiu, I. Gyacsok, X. P. Yuan, M. Drangova, D. B. Downey, and A. Fenster, "Fast prostate segmentation in 3D TRUS images based on continuity constraint using an autoregressive model," *Med. Phys.* **34**, 4109–4125 (2007).

⁹A. Ghanei, H. Soltanian-Zadeh, A. Ratkewicz, and F. F. Yin, "A three-dimensional deformable model for segmentation of human prostate from ultrasound images," *Med. Phys.* **28**, 2147–2153 (2001).

¹⁰L. X. Gong, S. D. Pathak, D. R. Haynor, P. S. Cho, and Y. Kim, "Parametric shape modeling using deformable superellipses for prostate segmentation," *IEEE Trans. Med. Imaging* **23**, 340–349 (2004).

¹¹K. Bogie, X. Wang, B. Fei, and J. Sun, "New technique for real-time inter-face pressure analysis: getting more out of large image data sets," *J. Rehabil. Res. Dev.* **45**, 523–535 (2008).

¹²X. Liu, D. L. Langer, M. A. Haider, Y. Yang, M. N. Wernick, and I. S. Yetik, "Prostate cancer segmentation with simultaneous estimation of Markov random field parameters and class," *IEEE Trans. Med. Imaging* **28**, 906–915 (2009).

¹³G. Lixin, S. D. Pathak, D. R. Haynor, P. S. Cho, and K. Yongmin, "Parametric shape modeling using deformable superellipses for prostate segmentation," *IEEE Trans. Med. Imaging* **23**, 340–349 (2004).

¹⁴B. Fei, H. Wang, J. D. Meyers, D. K. Feyes, N. L. Oleinick, and J. L. Duerk, "High-field magnetic resonance imaging of the response of human prostate cancer to P₄-based photodynamic therapy in an animal model," *Lasers Surg. Med.* **39**, 723–730 (2007).

¹⁵S. D. Pathak, D. R. Haynor, and Y. Kim, "Edge-guided boundary delineation in prostate ultrasound images," *IEEE Trans. Med. Imaging* **19**, 1211–1219 (2000).

¹⁶X. Yang and B. Fei, "3D prostate segmentation of ultrasound images combining longitudinal image registration and machine learning," *Medical Imaging: Image-Guided Procedures, Robotic Interventions, and Modeling*, edited by David R. Holmes III and Kenneth H. Wong, *Proc. SPIE* **8316**, 831620 (SPIE, San Diego, CA, 2012).

¹⁷I. B. Tutar, S. D. Pathak, L. X. Gong, P. S. Cho, K. Wallner, and Y. M. Kim, "Semiautomatic 3-D prostate segmentation from TRUS images using spherical harmonics," *IEEE Trans. Med. Imaging* **25**, 1645–1654 (2006).

¹⁸R. S. Xu, O. Michailovich, and M. Salama, "Information tracking approach to segmentation of ultrasound imagery of the prostate," *IEEE Trans. Ultrason. Ferroelectr. Freq. Control* **57**, 1748–1761 (2010).

¹⁹P. Yan, S. Xu, B. Turkbey, and J. Kruecker, "Adaptively learning local shape statistics for prostate segmentation in ultrasound," *IEEE Trans. Biomed. Eng.* **58**, 633–641 (2010).

²⁰B. Fei, D. Schuster, V. Master, H. Akbari, A. Fenster, and P. Nieh, "A molecular image-directed, 3D ultrasound-guided biopsy system for the prostate," *Medical Imaging: Image-Guided Procedures, Robotic Interventions, and Modeling*, edited by David R. Holmes III and Kenneth H. Wong, *Proc. SPIE* **8316**, 831613 (SPIE, San Diego, CA, 2012).

²¹X. Yang, D. Schuster, V. Master, P. Nieh, A. Fenster, and B. Fei, "Automatic 3D segmentation of ultrasound images using atlas registration and statistical texture prior," *Medical Imaging: Visualization, Image-Guided Procedures, and Modeling*, *Proc. SPIE* **7964**, 796432 (SPIE, San Diego, CA, 2011).

²²Y. Yu, J. A. Molloy, and S. T. Acton, "Segmentation of the prostate from suprapubic ultrasound images," *Med. Phys.* **31**, 3474–3484 (2004).

²³Y. Zhan and D. Shen, "Deformable segmentation of 3-D ultrasound prostate images using statistical texture matching method," *IEEE Trans. Med. Imaging* **25**, 256–272 (2006).

²⁴Y. Zhang, R. Sankar, and W. Qian, "Boundary delineation in transrectal ultrasound image for prostate cancer," *Comput. Biol. Med.* **37**, 1591–1599 (2007).

²⁵N. Hu, D. B. Downey, A. Fenster, and H. M. Ladak, "Prostate boundary segmentation from 3D ultrasound images," *Med. Phys.* **30**, 1648–1659 (2003).

²⁶A. C. Hodge, A. Fenster, D. B. Downey, and H. M. Ladak, "Prostate boundary segmentation from ultrasound images using 2D active shape models: Optimisation and extension to 3D," *Comput. Methods Programs Biomed.* **84**, 99–113 (2006).

²⁷C. Knoll, M. Alcaniz, V. Grau, C. Monserrat, and M. Carmen Juan, "Outlining of the prostate using snakes with shape restrictions based on the wavelet transform (Doctoral Thesis: Dissertation)," *Pattern Recogn.* **32**, 1767–1781 (1999).

- ²⁸T. C. Wang and N. B. Karayiannis, "Detection of microcalcifications in digital mammograms using wavelets," *IEEE Trans. Med. Imaging* **17**, 498–509 (1998).
- ²⁹S. G. Mallat, "A theory for multiresolution signal decomposition—The wavelet representation," *IEEE Trans. Pattern Anal. Mach. Intell.* **11**, 674–693 (1989).
- ³⁰Y. L. Qiao, J. S. Pan, and S. H. Sun, "An experimental comparison on gabor wavelet and wavelet frame based features for image retrieval," *Knowledge-Based Intelligent Information and Engineering Systems, Vol. 3683*, edited by R. Khosla, R. J. Howlett and L. C. Jain (Springer, Berlin/Heidelberg, 2005), pp. 353–358.
- ³¹M. Unser, "Texture classification and segmentation using wavelet frames," *IEEE Trans. Image Process.* **4**, 1549–1560 (1995).
- ³²A. Mojsilovic, M. Popovic, S. Markovic, and M. Krstic, "Characterization of visually similar diffuse diseases from B-scan liver images using non-separable wavelet transform," *IEEE Trans. Med. Imaging* **17**, 541–549 (1998).
- ³³V. N. Vapnik, *The Nature of Statistical Learning Theory* (Springer-Verlag, Berlin, 1995).
- ³⁴M. Brown, H. G. Lewis, and S. R. Gunn, "Linear spectral mixture models and support vector machines for remote sensing," *IEEE Trans. Geosci. Remote Sens.* **38**, 2346–2360 (2000).
- ³⁵H. Akbari, Y. Kosugi, K. Kojima, and N. Tanaka, "Hyperspectral image segmentation and its application in abdominal surgery," *International Journal of Functional Informatics and Personalised Medicine* **2**, 201–216 (2009).
- ³⁶T. L. Faber and E. M. Stokely, "Orientation of 3-D structures in medical images," *IEEE Trans. Pattern Anal. Mach. Intell.* **10**, 626–633 (1988).
- ³⁷N. M. Alpert, J. F. Bradshaw, D. Kennedy, and J. A. Correia, "The principal axes transformation—a method for image registration," *J Nucl. Med.* **31**, 1717–1722 (1990).
- ³⁸D. Cool, D. Downey, J. Izawa, J. Chin, and A. Fenster, "3D prostate model formation from non-parallel 2D ultrasound biopsy images," *Med. Image Anal.* **10**, 875–887 (2006).
- ³⁹I. B. Tutar, S. D. Pathak, L. Gong, P. S. Cho, K. Wallner, and Y. Kim, "Semiautomatic 3-D prostate segmentation from TRUS images using spherical harmonics," *IEEE Trans. Med. Imaging* **25**, 1645–1654 (2006).
- ⁴⁰H. Bustince, M. Pagola, E. Barrenechea, J. Fernandez, P. Melo-Pinto, P. Couto, H. R. Tizhoosh, and J. Montero, "Ignorance functions. An application to the calculation of the threshold in prostate ultrasound images," *Fuzzy Sets Syst.* **161**, 20–36 (2010).
- ⁴¹Y. Zhang, X. J. He, and J. H. Han, "Texture feature-based image classification using wavelet package transform," *Adv. Intell. Comput.*, Pt 1, **3644**, 165–173 (2005).

Akbari H, **Fei BW** (corresponding author). 3D ultrasound image segmentation using wavelet support vector machines, *Medical Physics* 2012; 39:2972-2984.

Copyright 2012 Am. Assoc. Phys. Med. One print or electronic copy may be made for personal use only. Systematic reproduction and distribution, duplication of any material in this paper for a fee or for commercial purposes, or modification of the content of the paper are prohibited.